Research Square

Preprints are preliminary reports that have not undergone peer review.
They should not be considered conclusive, used to inform clinical practice,
or referenced by the media as validated information.

Parametric Optimization of a Two-Dimensional Double Arc Star-Shaped Auxetic Unit Cell Using a Hybrid SEO Algorithm

Vladimir Sinđelić

sindjelic.v@mfkv.kg.ac.rs

University of Kragujevac

Research Article

Keywords: Arc star-shaped structure, Negative Poisson's ratio, Auxetic, Unit cell, Mechanical metamaterials, Structural optimization, Metaheuristic

Posted Date: November 13th, 2026

DOI: https://doi.org/10.21203/rs.3.rs-11577142/v1

License: This work is licensed under a Creative Commons Attribution 4.0 International License.
Read Full License

Additional Declarations: No competing interests reported.

Parametric Optimization of a Two-Dimensional Double Arc Star-Shaped Auxetic Unit Cell Using a Hybrid SEO Algorithm

Vladimir Sinđelić[1*]

[1]Faculty of Mechanical and Civil Engineering in Kraljevo, University of Kragujevac (Serbia)

*Corresponding author.

E-mail address: sindjelic.v@mfkv.kg.ac.rs (V. Sinđelić)

Abstract

Auxetic structures are a class of mechanical metamaterials characterized by a negative Poisson's ratio, which enables them to contract in the transverse direction when subjected to compression. Their mechanical response strongly depends on the geometry of the unit cell, making parametric optimization an important tool for improving their auxetic behavior. This study presents a procedure for optimizing the geometric parameters of a two-dimensional double arc star-shaped (2D-DASS) unit cell with the objective of minimizing its Poisson's ratio while maintaining Young's modulus, solid material volume, and total unit-cell volume within prescribed allowable deviations. The mechanical properties of the unit cell were determined analytically using Castigliano's second theorem in conjunction with Euler–Bernoulli beam theory. The optimization procedure was applied to seven initial configurations, with the initial angle θ ranging from 35° to 65° in increments of 5°. Five geometric parameters, namely θ, l_1, g, l_3, and t, were considered as design variables. The results showed that the optimized angle reached 70° in all considered cases, while the constraints on Young's modulus, solid material volume, and total unit-cell volume were satisfied within the prescribed allowable deviation of ±0.5%. For initial angles of 35°, 40°, and 45°, the optimization procedure produced negative Poisson's ratio values despite the positive values obtained from the initial analytical configurations. Furthermore, finite element analyses of structures composed of 3x3 unit cells demonstrated greater horizontal deformation in the optimized configurations under vertical compression. Comparisons between the analytical, optimization, and numerical results showed generally good agreement. The

findings demonstrate the potential of the proposed procedure for improving the auxetic response of 2D-DASS unit cells while preserving their principal mechanical and geometric characteristics.

Keywords: Arc star-shaped structure; Negative Poisson's ratio; Auxetic; Unit cell; Mechanical metamaterials; Structural optimization; Metaheuristic.

1. Introduction

Mechanical metamaterials are artificially engineered structures whose geometry and internal architecture are specifically designed to obtain existing or new mechanical properties that cannot be achieved in the same manner using conventional materials [1]. A particular group of mechanical metamaterials consists of structures with negative Poisson's ratio, known as auxetic structures. Unlike conventional materials, auxetic structures deform under loading in one direction in such a way that they simultaneously expand in the transverse direction. For example, under compression in the vertical direction, the dimension in the loading direction decreases while the dimension in the horizontal direction increases. This specific deformation behavior can contribute to enhanced energy absorption capability [2] , as well as other characteristic mechanical properties, making auxetic structures the subject of extensive research [1,3,4].

The fundamental building block of mechanical metamaterials is the unit cell, whose periodic repetition forms a structure of larger dimensions. In auxetic metamaterials, the negative Poisson's ratio is generally a consequence of the specific geometry of the unit cell and its deformation mechanism [3]. One of the characteristic geometrical configurations is represented by re-entrant structures, in which the elements of the unit cell are inclined inward toward the interior of the structure. Depending on the geometrical configuration, the inward re-entrant geometry can be realized in one or multiple directions, resulting in different deformation behaviors and Poisson's ratio values. Due to this characteristic behavior, such structures are frequently referred to in the literature as re-entrant and/or auxetic structures [1,3,5–7].

The term "auxetic" originates from the Greek word *auxetikos*, meaning something that increases [3]. Owing to their specific mechanical properties, auxetic structures have potential applications in various fields, including the

aerospace and automotive industries, protective and military systems, the textile industry, construction, and other areas where controlled deformation, energy absorption, or a specific combination of mechanical properties is desired [6] .

One of the particularly interesting geometries of auxetic structures is the star-shaped unit cell, which is re-entrant in both directions. The star-shaped unit cell consists of two vertical and two horizontal struts, as well as four arrow-shaped struts [8]. Owing to its geometry and depending on the values of its geometrical parameters, the Poisson's ratio of the star-shaped unit cell can be positive, zero, or negative, indicating that it exhibits a tunable Poisson's ratio [9].

For the analytical determination of the mechanical properties of star-shaped structures, Castigliano's second theorem was first applied in the study reported in [9]. Based on this theorem, expressions for the horizontal and vertical displacements were derived, from which the Poisson's ratio and Young's modulus were subsequently determined. In addition to conventional star-shaped unit cells, various other geometrical configurations of star-shaped unit cells have also been developed. In 2021, a structure consisting of arc segments connected by horizontal and vertical struts was introduced for the first time [10], and was referred to as an arc star-shaped structure. The analytical determination of its mechanical properties was also based on Castigliano's second theorem. In the study reported in [11], it was demonstrated that replacing the horizontal and vertical struts with tangent arcs results in greater absolute values of Poisson's ratio compared with the configuration presented in [10], while simultaneously reducing the structural mass. The application of Castigliano's second theorem for the analytical determination of the mechanical properties of star-shaped unit cells has also been reported in studies [12–14]. Thus, N. Feng et al. [13] validated the analytical model for determining the mechanical properties of a star-shaped arc unit cell through numerical and experimental analyses. H. Liu and L. Wang [12] demonstrated good agreement between the experimental and numerical results and the analytical results. Similar results for an arc star-shaped unit cell were also obtained by Z. Zheng et al. in [14]. Although these studies provided explicit analytical expressions for the mechanical properties, none of them investigated the optimization of the geometrical parameters of the unit cell with the aim of improving its mechanical properties.

The optimization of the geometrical parameters of auxetic structures was investigated by M. Zawistowski and A. Poteralski in studies [15,16] . For the optimization of the auxetic structures, they used the ANSYS software package, in which a genetic algorithm was implemented. In the first study [15], the objective of the optimization was to directly optimize the Poisson's ratio and maximum stress values using the finite element method, whereas in [16] the objective was to determine the maximum values of Young's modulus. H. Liu et al. [17] optimized the geometrical parameters of star-shaped unit cells with the aim of reducing their mass while increasing Young's modulus, subject to the constraint that the Poisson's ratio remains within the range of −0.03 to 0.03. A genetic algorithm was employed as the optimization method. In the study reported in [18], the geometry of the star-shaped unit cell presented in [9] was optimized using a genetic algorithm, with the objective of obtaining a Poisson's ratio as close to zero as possible. Another application of a genetic algorithm for the optimization of the geometrical parameters of a star-shaped unit cell was presented in [19]. The objective of the optimization was to minimize the mass of the unit cell while maintaining a negative Poisson's ratio within the range of −0.5 to −5. Hamid et al. [20] optimized the geometrical parameters of five different auxetic unit cells with the aim of obtaining the most negative possible Poisson's ratio. Four different metaheuristic optimization algorithms were employed, with the Flow Direction Algorithm (FDA) providing the best results.

A common feature of the studies dealing with the optimization of auxetic structures is that the imposed constraints were not strictly defined. This allowed the metaheuristic algorithms to explore a broader region of the design space during the optimization process. More strictly defined constraints for the optimization of a star-shaped auxetic unit cell were applied in the study [21]. The constraints were set to ensure that Young's modulus and relative density remained within ±1% of their prescribed target values. The Grey Wolf Optimizer (GWO) algorithm was used to optimize the geometric parameters of the unit cell, with the objective of minimizing the absolute value of Poisson's ratio.

The main objective of this study is to develop a procedure for optimizing the Poisson's ratio of the 2D double arc star-shaped (2D-DASS) unit cell using a metaheuristic optimization algorithm while simultaneously satisfying strictly defined constraints. The metaheuristic algorithm applied in this study does not represent a completely new optimization strategy in terms of introducing new fundamental search operators. Instead, the proposed approach

represents a hybrid methodology that combines and adapts several well-established mechanisms from the literature to the specific problem of parametric optimization of the 2D-DASS unit cell while simultaneously satisfying the defined constraints. The conceptual structure of the proposed approach is inspired by the search behavior of the Eye of Sauron, namely, the continuous scanning of the search space, identification of potential solutions, and their subsequent detailed investigation. Within the proposed methodology, the search-guidance hierarchy is based on the mechanism of the Grey Wolf Optimizer (GWO) [22], the candidate-position update employs the principle of Particle Swarm Optimization (PSO) [23], the concept of maintaining an external archive is adopted from evolutionary algorithms [24], the local search is based on the principles of memetic algorithms [25], while the dynamic tolerance mechanism is based on the concept of ε-constraints [26,27]. The novelty of the proposed approach lies in the specific combination, integration, and adaptation of these mechanisms into a unified optimization procedure specifically formulated for the parametric optimization of auxetic unit cells while simultaneously satisfying multiple strict constraints.

In Section 2, an analytical model was developed to determine the mechanical properties of the 2D-DASS unit cell, and a numerical example was performed for the defined geometric parameters, which were subsequently used for the optimization procedure presented in the following section. Section 3 describes the procedure and operating principle of the proposed optimization approach for auxetic unit cells. The results obtained using the analytical and optimization approaches are also compared. In Section 4, the obtained results are verified using the finite element method (FEM) for structures composed of 3x3 non-optimized and optimized 2D-DASS unit cells.

2. Design and analytical modeling of the unit cell

The geometry and design of the 2D-DASS unit cell are entirely adopted from the geometry of the 3D-DASS structure presented in [28]. Similar to the 3D-DASS structure, the 2D-DASS unit cell is defined by primary and derived geometric parameters, as illustrated in Fig. 1. The primary geometric parameters comprise all quantities required to define the geometry and construct the 2D-DASS unit cell. These parameters include the arc length l_1, arc length l_2, distance l_3 between arc 2 and the end of the 2D-DASS unit cell, angle θ between the vertical strut and the end of arc 1, and thickness t of the square cross-section. The derived geometric parameters represent the

quantities required for the analytical determination of the mechanical properties of the 2D-DASS structure. These parameters include the radius r of arc 1, the radius R of arc 2, the angle φ between the endpoints of arc 2, the angle α between the horizontal axis and radius r at the endpoint of arc 1, and L, which represents half of the total length of the unit cell [28]. Based on the geometric relationships shown in Fig. 1 and the expressions reported in [28], the derived geometric parameters can be expressed as functions of the primary geometric parameters as follows:

$$\alpha = \frac{\pi}{2} - \theta,\ \varphi = \frac{3}{2}\pi - 2\alpha = \frac{\pi}{2} + 2\theta,\ r = \frac{l_1}{\theta},\ R = \frac{l_2}{\varphi}, \tag{1}$$

where the angle θ is defined within the interval $30° \leq \theta \leq 70°$.

Based on the primary and derived geometric parameters, the half of the total length L of the 2D-DASS unit cell can be expressed as follows [28]:

$$L = l_3 + R + \left(r + R\right)\cos\alpha\,. \tag{2}$$

To ensure the geometric consistency of the 2D-DASS unit cell model, the following relationship is introduced:

$$l_2 = g l_1, \tag{3}$$

where g is a correction factor defined within the range $3/4 \leq g \leq 4/3$ [28].

Relative density ρ_r is one of the important parameters governing the mechanical properties of the unit cell. It is defined as the ratio between the volume of the solid material constituting the unit cell, V_C, and the total volume occupied by the unit cell, V_S. The expressions for calculating the volume of the solid material, the total volume of the 2D-DASS unit cell, and its relative density, as functions of the primary geometric parameters and the correction factor g, are given as follows:

$$V_C = 4\,\mathrm{t}^2\left(l_3 + l_1\left(2 + g + \frac{1}{\theta} + \frac{2g}{\pi + 4\theta}\right) - \frac{l_1\left(\pi + 2\left(2+g\right)\theta\right)\cos\theta}{\theta\left(\pi + 4\theta\right)}\right), \tag{4}$$

$$V_S = \frac{4t\left(\theta\left(2gl_1 + l_3\left(\pi + 4\theta\right)\right) + l_1\left(\pi + 2\left(2+g\right)\theta\right)\sin\theta\right)^2}{\theta^2\left(\pi + 4\theta\right)^2}, \tag{5}$$

$$\rho_r = \frac{V_C}{V_S} = \frac{\left(t\theta\left(\pi + 4\theta\right)\left(\begin{array}{l} l_3\theta\left(\pi + 4\theta\right) + l_1\left(\pi + \left(2+g\right)\left(2+\pi\right)\theta + 4\left(2+g\right)\theta^2\right) \\ -l_1\left(\pi + 2\left(2+g\right)\theta\right)\cos\theta \end{array}\right)\right)}{\left(\theta\left(2gl_1 + l_3\left(\pi + 4\theta\right)\right) + l_1\left(\pi + 2\left(2+g\right)\theta\right)\sin\theta\right)^2}. \tag{6}$$

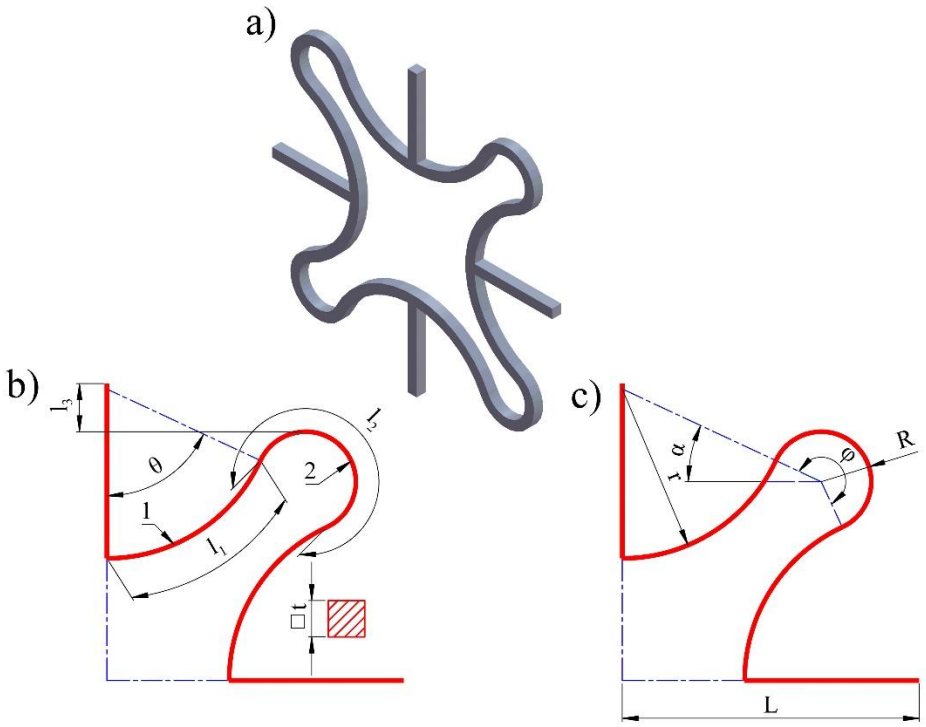


Fig. 1. 3D-DASS unit cell: (a) model, (b) primary geometric parameters, and (c) derived geometric parameters.

2.1. Poisson's ratio and Young's modulus

The analytical expressions for determining the Poisson's ratio and Young's modulus of the 2D-DASS structure are derived using Castigliano's second theorem in conjunction with the assumptions of Euler–Bernoulli beam theory. To analytically determine the Poisson's ratio and Young's modulus, the 3x3 array of 2D-DASS unit cells, shown in Fig. 2(a) and subjected to a vertical stress σ_Y, is reduced to a single unit cell, as shown in Fig. 2(b).

Owing to the symmetry of the unit cell, only one half of the unit cell subjected to the vertical F_Y, shown in Fig. 2(c), needs to be considered to determine the horizontal and vertical displacements. The half-unit cell is subsequently divided at point O into two parts, namely the left and right sides, as illustrated in Fig. 2(d). Consequently, unknown reactions arise at point O on the left and right sides. These reactions have equal magnitudes and opposite directions and consist of the vertical force Y_O and the bending moment M_O. When dividing the unit cell, the vertical force F_Y is assigned to one of the two sides; in the present case, the left side is considered.

To determine the unknown reactions, a system of equations is established by imposing the conditions that the sum of the vertical displacements of the left and right sides, f_{AY} and $f_{AY'}$, is equal to zero, and that the sum of the corresponding rotation angles, ϕ_A and $\phi_{A'}$, is also equal to zero, i.e.:

$$f_{AY'} + f_{AY} = 0,\ \phi_{A'} + \phi_A = 0. \tag{7}$$

Based on Castigliano's second theorem, the system of equations (7) can be written in the following form:

$$f_{AY'} + f_{AY} = \frac{1}{E \cdot I} \sum_i^3 \left(\int_0^{\gamma_i} M_{i'} \frac{\partial M_{i'}}{\partial Y_{O'}} \cdot r_i d\delta_{i'} + \int_0^{\gamma_i} M_{i'} \frac{\partial M_i}{\partial Y_O} \cdot r_i d\delta_i \right), \tag{8}$$

$$\phi_{A'} + \phi_A = \frac{1}{E \cdot I} \sum_i^3 \left(\int_0^{\gamma_i} M_{i'} \frac{\partial M_{i'}}{\partial Y_{O'}} \cdot r_i d\delta_{i'} + \int_0^{\gamma_i} M_{i'} \frac{\partial M_i}{\partial M_O} \cdot r_i d\delta_i \right), \tag{9}$$

where is the E Young's modulus of the material, I is the second moment of area of the square cross-section, given by $I=t^4/12$, δ_i denotes the arc length of the i-th segment, γ_i is the angle defining the orientation of the i-th segment, and r_i is the radius of the i-th segment. The quantities M_i and $M_{i'}$ represent the bending moments corresponding to each segment, while the bending moment M_i and $M_{i'}$ is determined from the following expression:

$$\begin{aligned}
M_{1'} &= M_{O'} + \left(Y_{O'} - F_Y\right) r \sin\delta_{1'} \\
M_{2'} &= M_{O'} + \left(Y_{O'} - F_Y\right)\left(\left(r+R\right)\sin\theta - R\cos\left(\delta_{2'} + \alpha\right)\right) \\
M_{3'} &= M_{O'} + \left(Y_{O'} - F_Y\right)\left(\left(r+R\right)\sin\theta - R\cos\left(\varphi + \alpha\right) + r\cos\theta - r\cos\delta_{3'}\right) \\
M_1 &= M_O - Y_O r \sin\delta_1, \\
M_2 &= M_O - Y_O\left(\left(r+R\right)\sin\theta - R\cos\left(\delta_2 + \alpha\right)\right), \\
M_3 &= M_O - Y_O\left(\left(r+R\right)\sin\theta - R\cos\left(\varphi + \alpha\right) + r\cos\theta - r\cos\delta_3\right).
\end{aligned} \tag{10}$$

By substituting the bending moment expressions given by Eq. (10) into Eqs. (8) and (9), the expressions for determining the unknown reactions are obtained as follows:

$$\begin{aligned}
Y_O &= \frac{F_Y}{2}, \\
M_O &= F_Y \frac{\left(\begin{array}{l} \left(\pi+4\theta\right)^2 l_1^2 + \left(\left(\pi+4\theta\right) l_1 + 2 l_2 \theta\right)\left(\begin{array}{l} \left(2 l_2 \theta + l_1\left(\pi+4\theta\right)\left(\theta-1\right)\right)\cos\theta \\ + \left(\begin{array}{l} \left(\pi+4\theta\right) l_1 \left(\theta-1\right) \\ + \left(2+\pi+4\theta\right) 12\theta \end{array}\right)\sin\theta \end{array}\right) \end{array}\right)}{2\left(\pi+4\theta\right)^2\left(2 l_1 + l_2\right)\theta^2}.
\end{aligned} \tag{11}$$

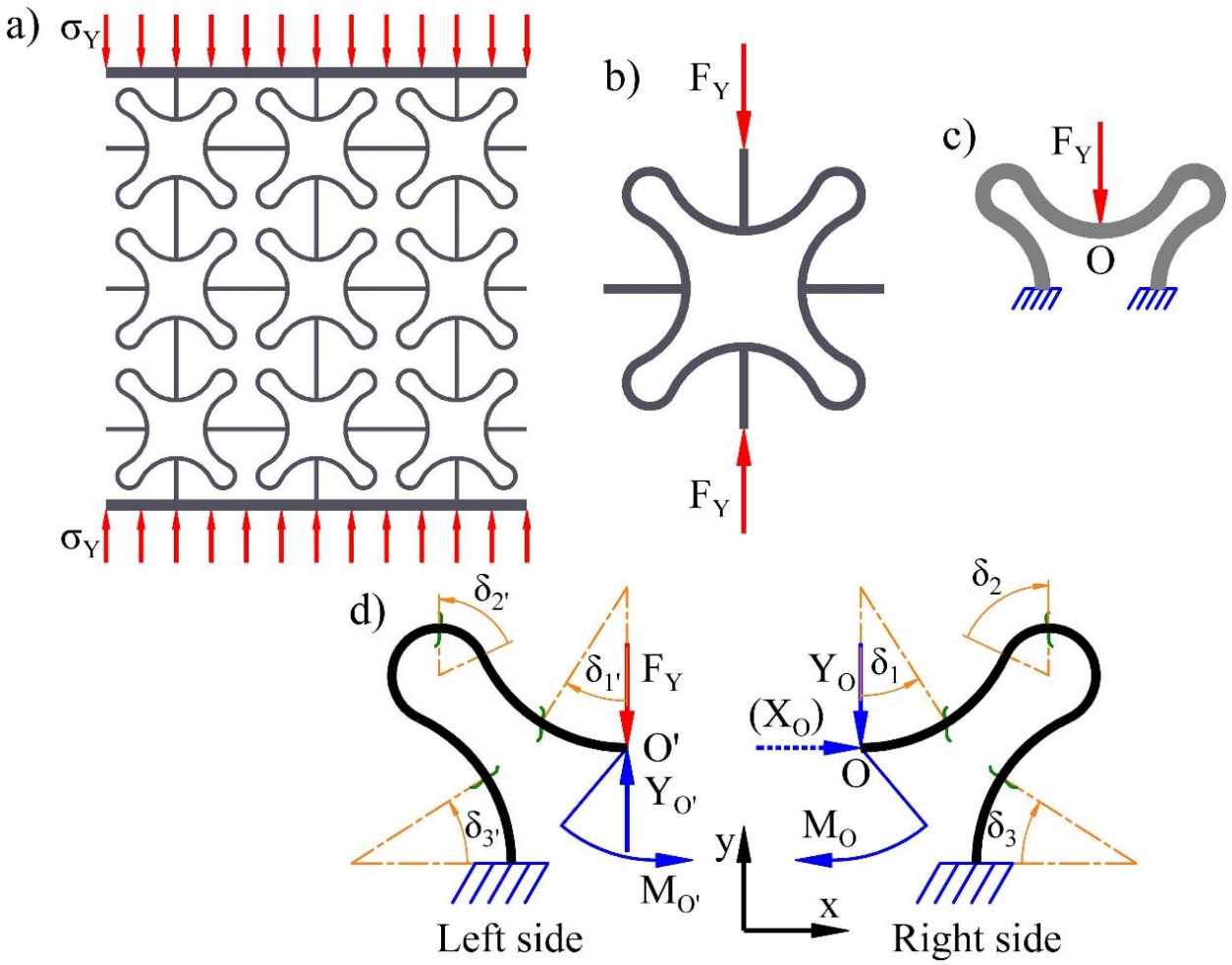


Fig. 2. Analytical model: (a) 3x3 structure, (b) vertical loading of the unit cell, (c) half of the unit cell, and (d) free-body diagram.

To determine the horizontal and vertical displacements, it is sufficient to consider the right half of the unit cell (see Fig.2 (d)). For the determination of the horizontal displacement, an auxiliary horizontal force X_O, whose magnitude is set equal to zero, is introduced. By applying Castigliano's second theorem, the expressions for calculating the horizontal f_X and vertical f_Y displacements are obtained as follows [11,28,29]:

$$f_X = \frac{1}{E \cdot I} \sum_i^3 \left(\int_0^{\gamma_i} M_{i'} \frac{\partial M_i}{\partial X_O} \cdot r_i d\delta_i \right) \Bigg|_{X_O=0}, \tag{12}$$

$$f_Y = \frac{1}{E \cdot I} \sum_i^3 \left(\int_0^{\gamma_i} M_{i'} \frac{\partial M_i}{\partial Y_O} \cdot r_i d\delta_i \right) \Bigg|_{X_O=0}. \tag{13}$$

Due to the introduction of the additional horizontal force, the expressions for the bending moments take the following form:

$$\begin{aligned}
M_1 &= M_O - Y_O r\sin\delta_1 - X_O r\left(1-\cos\delta_1\right),\\
M_2 &= M_O - Y_O\left(\left(r+R\right)\sin\theta - R\cos\left(\delta_2+\alpha\right)\right) -\\
&\quad X_O\left(r - r\cos\theta - R\sin\alpha + R\sin\left(\delta_2+\alpha\right)\right),\\
M_3 &= M_O - Y_O\left(\left(r+R\right)\sin\theta - R\cos\left(\varphi+\alpha\right) + r\cos\theta - r\cos\delta_3\right)\\
&\quad - X_O\left(r - \left(r+R\right)\cos\theta - \left(r+R\right)\sin\theta + r\sin\delta_3\right).
\end{aligned} \tag{14}$$

By substituting the bending moment expressions given by Eq. (14) into Eqs. (12) and (13), the analytical expressions for calculating the horizontal f_X and vertical f_Y displacements are obtained as follows:

$$f_X = \frac{3F_Y l_1^3\begin{pmatrix}32\theta^4 C_{X1} - 8\pi^3\theta C_{X2} - 64\pi\theta^3 C_{X3} - \pi^4 C_{X4} - 8\pi^2\theta^2 C_{X5}\\ +\left(\pi+2(2+g)\theta\right)\left(C_{X6} - C_{X7} + C_{X8} - C_{X9}\right)\end{pmatrix}}{E\left(2+g\right)t^4\theta^4\left(\pi+4\theta\right)^4}, \tag{15}$$

$$f_Y = \frac{6F_Y l_1^3\left(C_{Y1} + 16\pi\theta^3 C_{Y2} + 2\pi^2\theta^2 C_{Y3} + \left(\pi+2\left(2+g\right)\theta\right)\left(C_{Y4} + C_{Y5} - C_{Y6} + C_{Y7}\right)\right)}{E\left(2+g\right)t^4\theta^4\left(\pi+4\theta\right)^4}, \tag{16}$$

where C_{Xi} and C_{Yi}, for i=1,…9, denote the coefficients whose values are given in the Appendix.

Based on the expressions derived above, the Poisson's ratio v and Young's modulus E_Y of the 2D-DASS unit cell can be calculated as follows [11,28]:

$$v = -\frac{\varepsilon_X}{\varepsilon_Y} = -\frac{f_X}{f_Y}\cdot\frac{L_Y}{L_X} = \frac{\begin{matrix}C_{X4}\pi^4 + 8C_{X2}\pi^3\theta + 8C_{X5}\pi^2\theta^2 + 64C_{X3}\pi\theta^3 - 32C_{X1}\theta^4\\ -\left(\pi+2\left(2+g\right)\theta\right)\left(C_{X6} - C_{X7} + C_{X8} - C_{X9}\right)\end{matrix}}{2\begin{pmatrix}C_{Y1} + 2C_{Y3}\pi^2\theta^2 + 16C_{Y2}\pi\theta^3 + \left(\pi+2\left(2+g\right)\theta\right)\\ \left(C_{Y4} + C_{Y5} - C_{Y6} - C_{Y7}\right)\end{pmatrix}}, \tag{17}$$

$$E_Y = \frac{\sigma_Y}{\varepsilon_Y} = \frac{F/A}{f_Y/L_Y} = \frac{F_Y}{4\cdot f_Y\cdot t}\cdot\frac{L_Y}{L_X} = \frac{E\left(2+g\right)t^3\theta^4\left(\pi+4\theta\right)^4}{12l_1^3\begin{pmatrix}C_{Y1} + 2C_{Y3}\pi^2\theta^2 + 16C_{Y2}\pi\theta^3 + \left(\pi+2\left(2+g\right)\theta\right)\\ \left(C_{Y4} + C_{Y5} - C_{Y6} - C_{Y7}\right)\end{pmatrix}}, \tag{18}$$

where ε_X and ε_Y denote the horizontal and vertical strains, respectively, L_X and L_Y are the width and height of the 2D-DASS unit cell, respectively, and A denotes the cross-sectional area, defined as $A=2Lt$.

2.2. Numerical example

For further analysis, the following values of the primary geometric parameters were adopted: l_1=20 mm, t=2 mm, l_3=5 mm, and g=1, while the angle θ was varied from 30° to 70°. The Young's modulus of the base material was set to E=1500 MPa [11,28]. Based on the adopted geometric parameters and Eqs. (6), (17), and (18), the mechanical properties of the 2D-DASS unit cell were determined, and the corresponding results are presented in Fig. 3.

As the angle (\theta) increases, the relative density of the 2D-DASS unit cell increases, as shown in Fig. 3(a). At the same time, an increase in θ results in a decrease in the Poisson's ratio, indicating more pronounced auxetic behavior of the 2D-DASS unit cell at higher values of θ, as shown in Fig. 3(b). The limiting value of the angle θ, at which the Poisson's ratio reaches zero, is 45.8975°. As can be clearly observed in Fig. 3(c), increasing the angle θ also leads to an increase in the Young's modulus of the 2D-DASS unit cell.

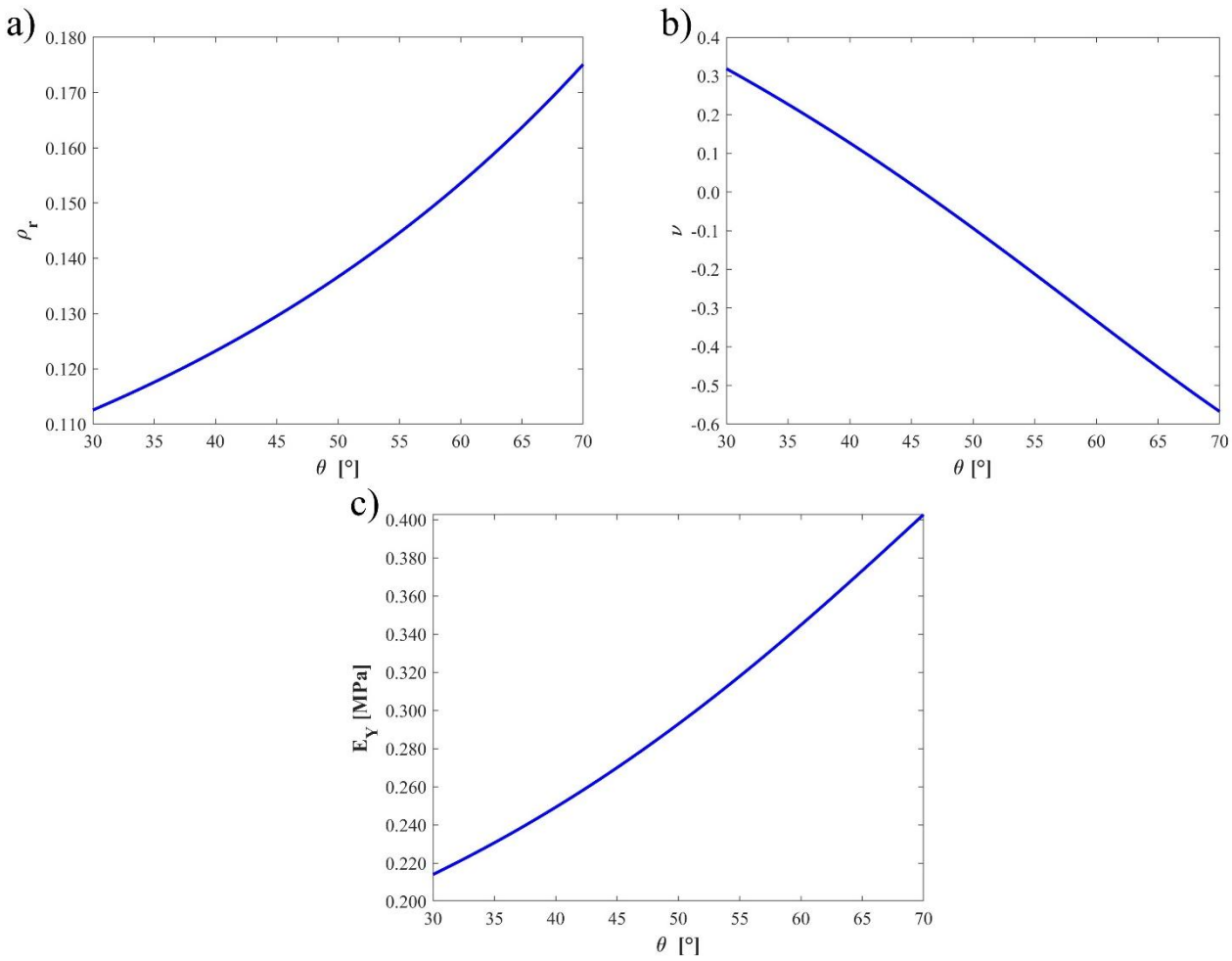


Fig. 3. Analytical results for the 2D-DASS unit cell: (a) relative density ρ_r, (b) Poisson's ratio v and (c) Young's modulus E_Y as functions of the angle θ.

3. Optimization Problem and the Sauron's Eye Optimization (SEO) Algorithm

The objective of the optimization is to determine the geometric parameters of the 2D-DASS unit cell such that the minimum value of the Poisson's ratio is achieved while simultaneously maintaining the Young's modulus E_Y, the unit cell volume V_C, and the volume of the space occupied by the unit cell V_S within a tolerance of ±0.5% of their respective reference values [21]. The vector of design variables is defined as:

$$\mathrm{x} = \left[\theta, l_1, g, l_3, t\right], \tag{19}$$

where the lower and upper bounds of the design variables are defined as follows:

$$\begin{aligned} &30° \le \theta \le 70°, \\ &1 \le l_1 \le 30, \\ &\frac{3}{4} \le g \le \frac{4}{3}, \\ &1 \le l_3 \le 30, \\ &0.5 \le t \le 5. \end{aligned} \tag{20}$$

The optimization problem can be formulated as follows:

$$\min_{x} \; f\left(x\right) = \nu\left(x\right), \tag{21}$$

subject to the following constraints:

$$\left|\frac{E_Y\left(x\right) - E_Y^t}{E_Y^t}\right| \le \varepsilon, \; \left|\frac{V_C\left(x\right) - V_C^t}{V_C^t}\right| \le \varepsilon, \; \left|\frac{V_S\left(x\right) - V_S^t}{V_S^t}\right| \le \varepsilon, \tag{22}$$

where E_Y^t, V_C^t, and V_S^t denote the target values of the Young's modulus, unit cell volume, and volume of the space occupied by the unit cell, respectively, while ε represents the allowable relative deviation from the target values, which is set to ±0.5% in the present study.

3.1. Sauron's Eye Optimization (SEO) Algorithm

The inspiration for the newly proposed optimization strategy for determining the geometric parameters of the 2D-DASS unit cell was derived from the concepts presented in the epic fantasy novel The Lord of the Rings. The

conceptual framework of the proposed strategy consists of three main entities: the Eye of Sauron, the Nazgûl, and the One Ring, whose characteristic behaviors and interactions are used to define the search mechanism within the optimization space. In the proposed conceptual framework, the Eye of Sauron continuously searches the space, i.e., scans the search domain for the potential presence of the One Ring. When a potential location of the Ring is detected during the search, the Eye of Sauron sends its agents, the Nazgûl, to investigate the detected location in greater detail. If the Nazgûl confirm the presence of the One Ring, they locate it and bring it back to the Eye of Sauron.

To simulate and mathematically describe the conceptual story from the novel within the optimization process, the SEO algorithm is divided into three fundamental mechanisms for identifying high-quality solutions during the optimization of the geometric parameters of the 2D-DASS unit cell:

1) scanning the solution space using the Eye,

2) storing feasible solutions in the Eye's archive, and

3) local search and guidance performed by the Nazgûl, i.e., the agents.

The Eye does not aim to directly identify the best solution. Instead, it continuously explores the solution space and identifies candidate solutions that satisfy the predefined constraints. In the considered optimization problem, a solution is regarded as feasible when the values of the constrained quantities remain within the prescribed tolerance of ±0.5% with respect to their corresponding reference values. These feasible candidates are subsequently stored and maintained in the Eye's archive. The Nazgûl, i.e., the agents, then perform a local search in the neighborhoods of the archived candidates with the aim of identifying new feasible solutions while simultaneously seeking lower values of the Poisson's ratio.

The SEO algorithm was implemented in the MATLAB programming environment. Prior to the main iterative loop, the target values of the constraints, E_Y^t, V_C^t, and V_S^t, are defined, together with the fixed parameter representing the Young's modulus of the base material, E=1500 MPa. Subsequently, the main parameters of the SEO algorithm are specified. The maximum number of iterations is set to 500, while 200 potential solutions are

generated and evaluated in each iteration. From these potential solutions, the 25 best feasible candidates are stored in the Eye's archive.

Next, a vector of five design variables, θ, l_1, g, l_3 and t, is defined, with their lower and upper bounds specified by Eq. (20). Following the definition of the design variables, the initial population is generated. At this stage, the initial population is uniformly randomly initialized within the prescribed bounds of the design variables according to the following expression:

$$x_{i,j} = L_j + r_{i,j}\left(U_j - L_j\right), \tag{23}$$

where $x_{i,j}$ denotes the value of the j-th design variable for the i-th candidate, L_j and U_j represent the lower and upper bounds of the j-th design variable, respectively and $r_{i,j}\epsilon(0,1)$ is a random number generated from a uniform distribution over the interval [0,1]. The index i=1,…200 denotes the candidate index, while j=1,…5 represents the design variable index.

Following the initialization, the SEO algorithm enters the main iterative loop, which is executed until the predefined maximum number of iterations N_{max} is reached, set to 500 in the present study. In each iteration, the prescribed constraints are evaluated, the archive of feasible solutions is updated, and a local search of the surrounding solution space is performed. Based on the best solution identified up to that point, a new population is generated, thereby progressively directing the search toward the optimal region of the design variable space.

At the beginning of the main loop of the SEO algorithm, a dynamic constraint tolerance is introduced to enable a gradual transition from a broader to a more precise search region [27]. During the first half of the total number of iterations, the algorithm explores the solution space using a tolerance that linearly decreases from an initial allowable deviation of ±5% to the final target tolerance of ±0.5%. In the second half of the iterative process, the tolerance remains constant at the final value of ±0.5%, allowing the algorithm to focus exclusively on refining the candidate solutions strictly within the prescribed constraints given by Eqs. (22). The evolution of the constraint tolerance throughout the iterative process is illustrated in Fig. 4 and is mathematically defined as follows [26,27]
:

$$\tau_N = \begin{cases} \tau_f + (\tau_0 - \tau_f)\left(1 - \dfrac{N}{0.5N_{\max}}\right), & if\ N \le 0.5N_{\max} \\ \tau_f, & if\ N > 0.5N_{\max} \end{cases}, \tag{24}$$

where N denotes the current iteration of the algorithm, N_{max} is the maximum number of iterations, τ_0 is the initial tolerance, τ_f is the final tolerance, and τ_N represents the current tolerance at iteration N.

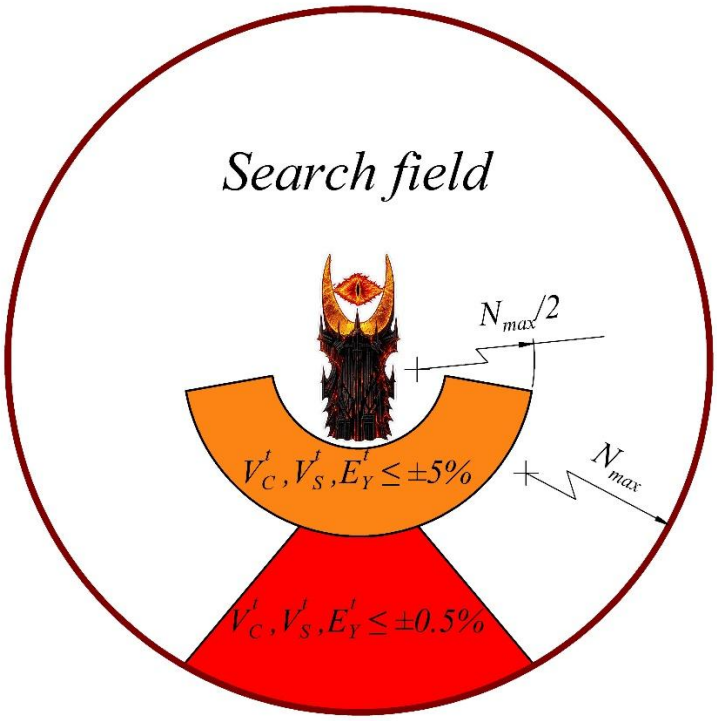


Fig. 4. Sauron's Eye searching the constraint space using dynamic tolerance.

3.2. Scanning Phase of the SEO Algorithm

In the first phase of the algorithm, the Eye performs a global search of the solution space by scanning 200 potential candidates in each iteration. Each candidate x_i is defined by the vector of design variables x_i=[θ, l_1, g, l_3, t]. For each scanned candidate, the mechanical properties $E_Y(x_i)$, $V_C(x_i)$, $V_S(x_i)$ and $\nu(x_i)$. are calculated using the analytical expressions derived in Section 2. Subsequently, the relative deviations of the constrained quantities from their respective target values are determined as follows:

$$\Delta_{E_Y}^{(i)} = \frac{E_Y(x) - E_Y^t}{E_Y^t},\ \Delta_{V_C}^{(i)} = \frac{V_C(x) - V_C^t}{V_C^t},\ \Delta_{V_S}^{(i)} = \frac{V_S(x) - V_S^t}{V_S^t}. \tag{25}$$

A candidate x_i is considered a feasible solution if the absolute values of all three relative deviations are less than or equal to the current value of the dynamic tolerance τ_N:

$$\left|\Delta_{E_Y}^{(i)}\right| \le \tau_N,\ \left|\Delta_{V_C}^{(i)}\right| \le \tau_N,\ \left|\Delta_{V_S}^{(i)}\right| \le \tau_N. \tag{26}$$

All values of the design variables that satisfy the prescribed conditions are temporarily stored together with their corresponding Poisson's ratio values v_i. This list represents the set of feasible solutions identified by the Eye of Sauron during the current iteration. Upon completion of the scanning phase, the Eye's archive is updated. The temporary list is sorted in ascending order according to the Poisson's ratio v_i, giving priority to solutions with lower Poisson's ratio values.

Following the sorting procedure, the mechanical properties of each feasible candidate are recalculated and the fulfillment of the constraint conditions is re-evaluated, thereby eliminating any potential deviations that may have occurred during the scanning process. Since the Eye's archive can contain a maximum of 25 best feasible solutions, newly identified feasible solutions are directly added if the archive is not yet full. If the archive is already full, each new candidate is evaluated to determine whether its Poisson's ratio represents an improvement over that of the worst solution currently stored in the archive. If the Poisson's ratio v_i of the new candidate is lower than that of the worst archived solution, the new candidate replaces the existing worst solution (see Fig.5). In this manner, throughout the entire optimization process, the Eye's archive continuously maintains the 25 best feasible solutions identified up to the current iteration [30,31] .

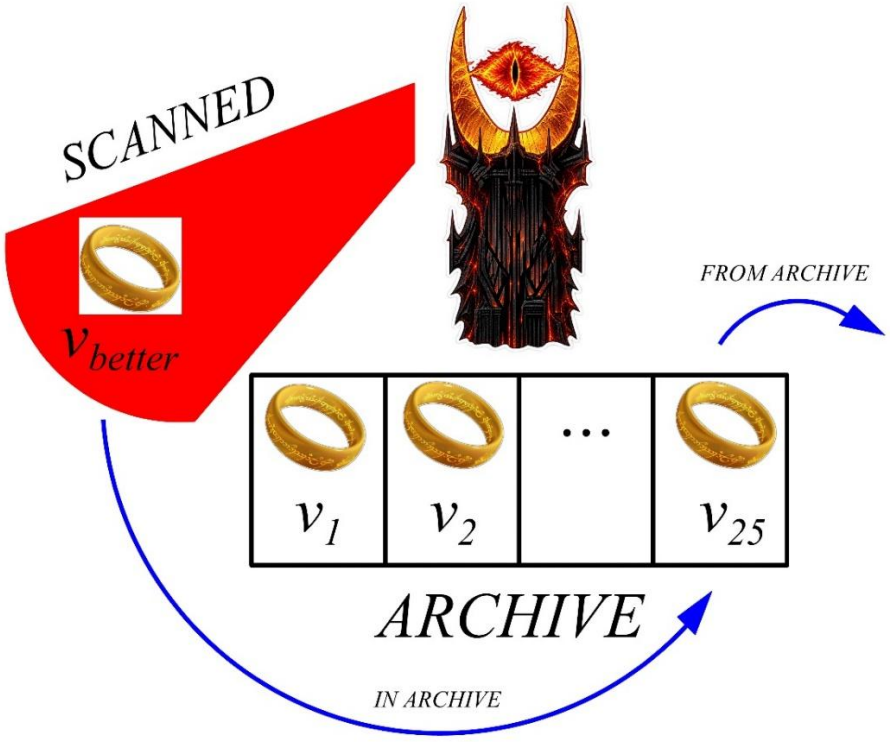


Fig. 5. Archiving process of the SEO algorithm.

3.3. Local Search and Guidance of the Nazgûl

If the Eye of Sauron's archive is not empty, the algorithm proceeds to the next stage, namely the local search performed by the Nazgûl, the agents of Sauron. The objective of this stage is to thoroughly explore the region in the immediate vicinity of the previously identified feasible solutions in order to identify new solutions with even lower values of the Poisson's ratio while simultaneously satisfying all prescribed constraints [25] .

For each solution x_n stored in the archive, the agents, i.e., the Nazgûl, generate a new candidate solution $x_{n,new}$ by applying a random perturbation [25]:

$$x_{n,new} = x_n + \varepsilon_j \rightarrow \varepsilon_j \in \left[\left(-0.01\left(U_j - L_j\right)\right), \left(0.01\left(U_j - L_j\right)\right)\right], \tag{27}$$

where ε_j denotes the perturbation of the j-th design variable, while U_j and L_j represent its upper and lower bounds, respectively. The perturbation amplitude is limited to ±2% of the range of each design variable, ensuring that the local search remains focused on the immediate neighborhood of the archived solution x_{arhive}.

For each new candidate solution $x_{n,new}$, the mechanical properties E_Y, V_C, V_S and v are calculated using the analytical expressions given in Section 2. The feasibility of the newly generated solutions is evaluated in the same manner as in the scanning phase, using Eqs. (25) and (26). If the new candidate solution $x_{n,new}$ satisfies all prescribed constraints, it is temporarily archived together with its corresponding Poisson's ratio value $v_{n,new}$.

After all agents complete the local search, the best solution among the newly generated feasible candidates is selected, i.e., the solution with the lowest Poisson's ratio. If its Poisson's ratio is lower than that of the current best solution x_{best}, it is designated as the new global best solution and stored as x_{best}. Fig. 6. schematic representation of the local search procedure performed by the Nazgûl.

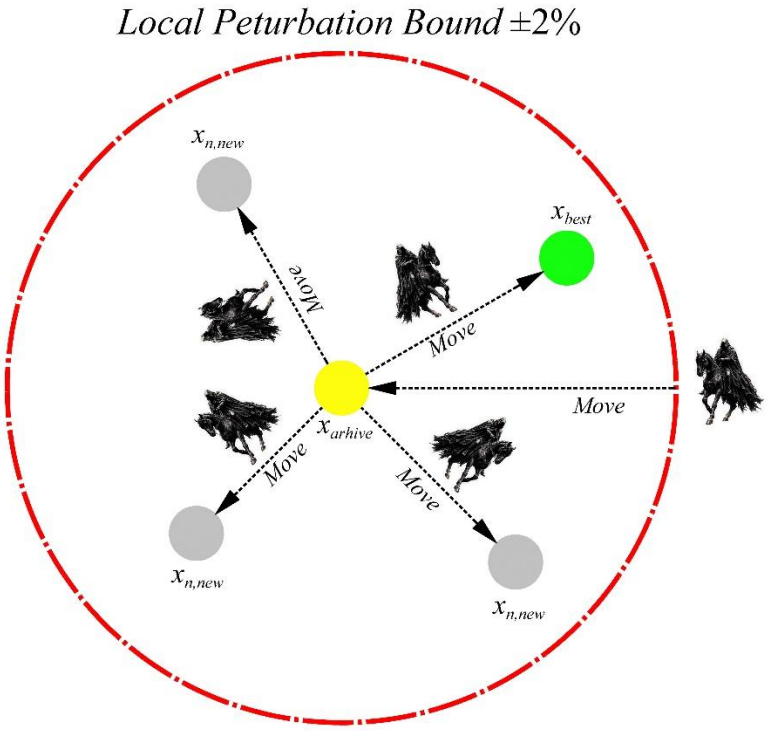


Fig. 6. Local search of the Nazgûl around an archived solution of the Eye of Sauron.

Upon completion of the local search, the population is updated for the next iteration. If a new global best solution x_{best} is identified during the local search, all population members are guided toward it according to the following expression [22,23] :

$$x_{i,new} = x_i + r\left(x_{best} - x_i\right), \tag{28}$$

where r is a random number drawn from a uniform distribution over the interval [0,1]. In this manner, each candidate x_i in the population is assigned a new position representing a linear combination of its current position and that of the global best solution, while the random factor r introduces stochasticity into the population guidance process.

If no new global best solution is identified during the local search, the population is guided toward the best solution stored in the Eye's archive, x_{arhive}, according to the following expression [22,23] :

$$x_{i,new} = x_i + r\left(x_{arhive} - x_i\right). \tag{29}$$

If the archive is empty, which may occur during the early iterations when the dynamic tolerance is still relatively broad, the population is randomly perturbed to enable further exploration of the solution space:

$$x_{i,new} = x_i + 0.5\left(U - L\right)\left(r - 0.5\right), \tag{30}$$

where U and L denote the vectors of the upper and lower bounds of the design variables, respectively. All newly generated solutions are subsequently projected onto the allowable interval $[L_j, U_j]$, ensuring that the values of the design variables remain within their prescribed bounds.

The entire process, comprising solution-space scanning, local search, archive updating, and population updating, is repeated iteratively until the predefined maximum number of iterations N_{max} is reached. The pseudocode of the SEO algorithm is presented in Fig. 7.

1: Initialize population x_i ($i = 1, 2, ..., P$)

2: Initialize archive, $x_{best} = \emptyset$, $v_{best} = \infty$

3: Initialize algorithm parameters (N_{max}, P, K, τ_0, τ_f)

4: For each iteration $N = 1$ to N_{max} do

5: Compute dynamic tolerance τ_N

6: For each candidate x_i in population do

7: Compute E_Y, V_C, V_S and v

8: Evaluate feasibility using Eq. (26)

9: End For

10: Update archive with K best feasible solutions

11: Perform local search by Nazgûl agents around archived solutions

12: Update x_{best} if a better solution is found

13: Update population toward x_{best} or best archived solution

14: Record history $v_{best}(N) = v_{best}$

15: End For

16: Return x_{best} and v_{best}

Fig. 7. Pseudocode of the Sauron's Eye Optimization (SEO) algorithm.

3.4. Numerical example

The optimization of the geometric parameters of the 2D-DASS unit cell was performed for values of the angle θ ranging from 35° to 65°, while the remaining geometric parameters were defined in Section 2.2. Figure 8 presents the convergence curves of the SEO algorithm over 500 iterations for θ=40° and θ=60°. The presented convergence curves show that, during the initial iterations, the SEO algorithm intensively explores the search space, which is reflected in pronounced variations in the objective-function value, represented by the Poisson's ratio in the present optimization problem. As the number of iterations increases, the search process gradually transitions from the exploration phase to the local exploitation phase. During this stage, the objective function value is further reduced, and the algorithm converges toward an optimal solution while satisfying the prescribed constraints.

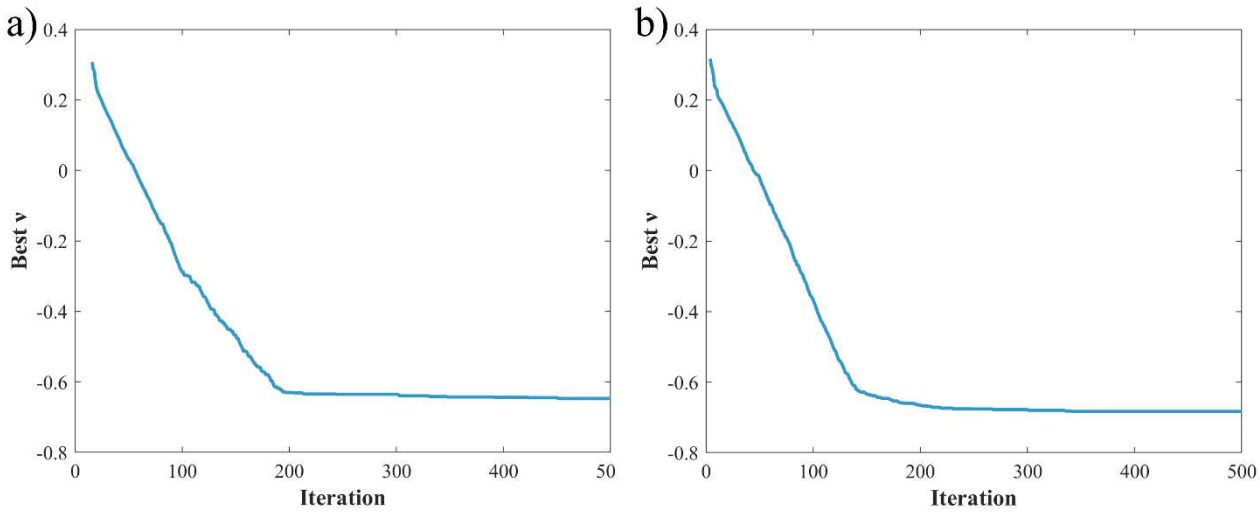


Fig. 8. Convergence curves of the SEO algorithm for: (a) θ=40° and (b) θ=60°.

Table 1 presents the values of the non-optimized (θ, l_1, g, l_3, t) and optimized (θ_{opt}, l_{1opt}, g_{opt}, l_{3opt}, t_{opt}) geometric parameters of the 2D-DASS unit cell. The values of l_2 and l_{2opt} are calculated using Eq. (3). It can be observed that, for all considered initial values of the angle θ, the optimized angle θ_{opt} is equal to 70°, i.e., it reaches the upper bound of the prescribed interval. The optimized values of the arc lengths l_{1opt} and l_{2opt} range from 16.8700 mm to 22.7386 mm, while the value of l_{3opt} is greater than 5 mm in all considered cases. On the other hand, the thickness of the optimized 2D-DASS unit cell, t_{opt}, is lower than that of the non-optimized unit cell, i.e., lower than 2 mm, in all cases. The optimized correction factor g_{opt} ranges from 0.75 to 1.1545. For the unit cells with initial angle values of θ=55° and θ=60°, the optimized correction factor reaches the lower bound of the prescribed interval, namely g_{opt} =3/4.

Table 1. Geometric parameters of the non-optimized and optimized 2D-DASS unit cells.

Non-optimized geometric parameters						***Optimized geometric parameters***					
θ [°]	l_1 [mm]	l_3 [mm]	g	t [mm]	l_2 [mm]	θ_{opt} [°]	l_{1opt} [mm]	l_{3opt} [mm]	g_{opt}	t_{opt} [mm]	l_{2opt} [mm]
35	20	5	1	2	20	70	21.0213	9.8561	1.0755	1.7978	22.6074
40	20	5	1	2	20	70	22.7730	9.7706	0.8258	1.8059	18.8052
45	20	5	1	2	20	70	22.3774	8.9019	0.8542	1.8421	19.1150
50	20	5	1	2	20	70	22.5373	8.2663	0.8077	1.8690	18.2025
55	20	5	1	2	20	70	22.7386	7.7450	0.7500	1.8928	17.0539
60	20	5	1	2	20	70	22.4933	6.9104	0.7500	1.9242	16.8700

65	20	5	1	2	20	70	19.1060	5.6225	1.1545	1.9819	22.0572

The mechanical properties of the non-optimized and optimized 2D-DASS unit cells for the considered range of the angle θ are presented in Table 2. As can be observed, the optimized values of V_C, V_S, and E_Y remain within the prescribed allowable deviation of ±0.5%. The relative density values of the optimized 2D-DASS unit cells were determined using Eq. (6). The largest deviations in relative density with respect to the non-optimized geometric parameters were observed for the initial angle values of θ =40° and θ =65°, amounting to 0.8929% and -0.6720%, respectively. These deviations exceed the prescribed limit of ±0.5% because the corresponding values of V_C and V_S are located close to the limiting values of the allowable ±0.5% deviation. The SEO algorithm successfully identified the lowest Poisson's ratio values for all considered values of the angle (\theta) within the prescribed interval, while the constraints on V_C, V_S, and E_Y were satisfied within the allowable deviation of ±0.5%. Of particular significance is that, for the initial angle values of θ =35°, 40° and 45°, for which positive Poisson's ratio values were obtained using the analytical approach, negative values were obtained after optimization. At the same time, the Young's modulus, and thus the stiffness of the unit cell, was maintained within the prescribed allowable deviation. The relationship between the non-optimized and optimized geometric parameters is additionally presented graphically in Fig. 9.

Table 2. Mechanical properties of the 2D-DASS unit cell obtained using analytical and optimization approaches.

θ [°]		***35***	***40***	***45***	***50***	***55***	***60***	***65***
V_C [mm^3]	***Analytical***	1155.46	1172.47	1189.17	1205.46	1221.24	1236.44	1250.98
	SEO	1157.53	1167.09	1193.90	1210.94	1222.67	1238.79	1253.76
	Error [%]	+0.1790	-0.4593	+0.3974	+0.4548	+0.1171	+0.1899	+0.2220
V_S [mm^3]	***Analytical***	9827.50	9515.39	9179.64	8822.01	8444.73	8050.43	7642.00
	SEO	9817.42	9556.68	9207.75	8844.94	8484.03	8061.11	7606.61
	Error [%]	-0.1025	+0.4339	+0.3062	+0.2599	+0.4653	+0.1327	-0.4632
ρ_r	***Analytical***	0.1175	0.1232	0.1295	0.1366	0.1446	0.15359	0.1637
	SEO	0.1179	0.1221	0.1297	0.1369	0.1441	0.1537	0.1648
	Error [%]	-0.3404	+0.8929	-0.1544	-0.2196	0.3458	-0.0716	-0.6720
E_Y [MPa]	***Analytical***	0.2306	0.2493	0.2700	0.2929	0.3179	0.3448	0.3733
	SEO	0.2300	0.2498	0.2694	0.2924	0.3188	0.3460	0.3740
	Error [%]	-0.2555	+0.1843	-0.2098	-0.1697	+0.2779	+0.3419	+0.1863
v	***Analytical***	0.2268	0.1271	0.0200	-0.0936	-0.2121	-0.3331	-0.4530

SEO	-0.5347	-0.6473	-0.6340	-0.6558	-0.6831	-0.6831	-0.5015

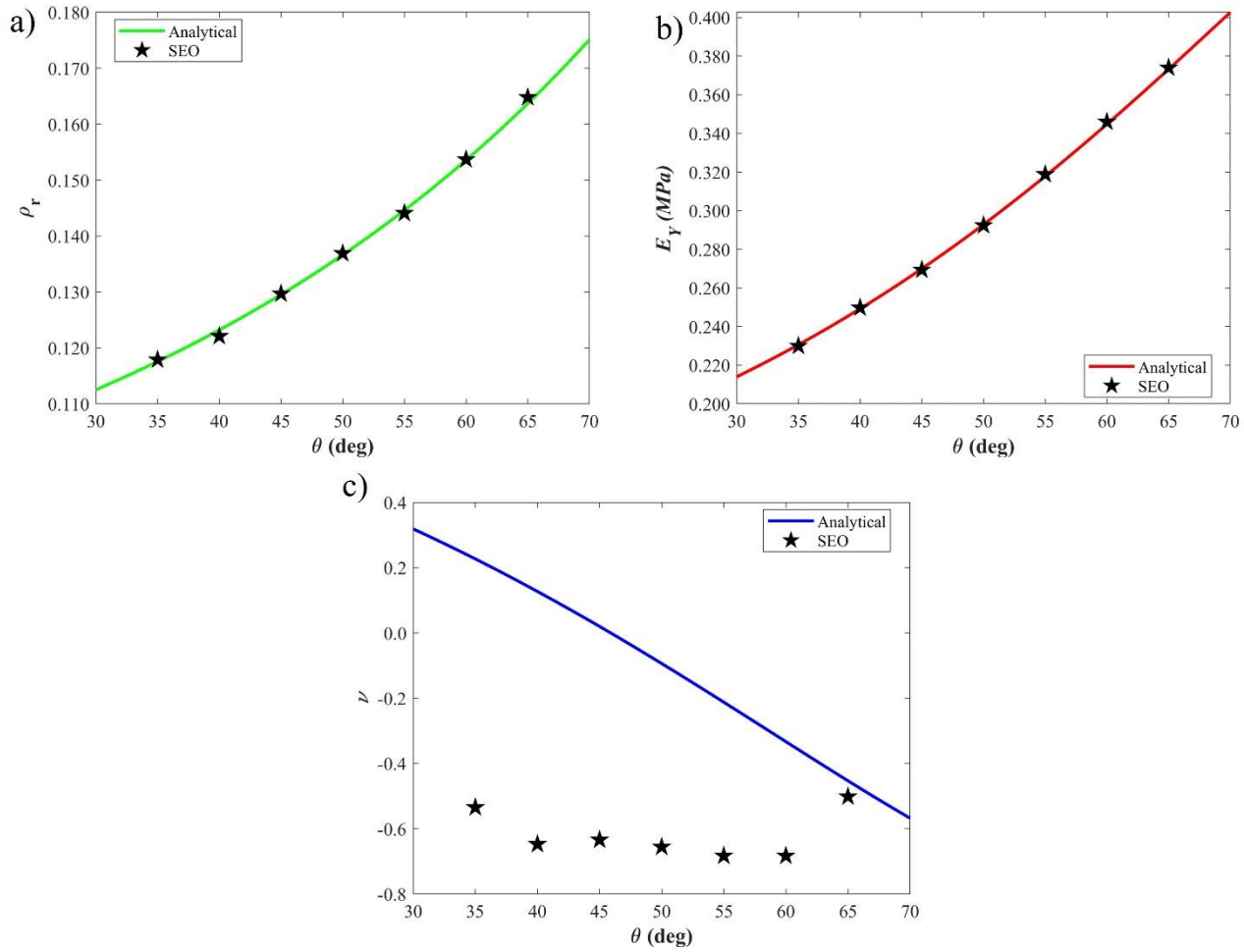


Fig. 9. Analytical results versus SEO-optimized results: (a) relative density ρ_r, (b) Young's modulus E_Y, and (c) Poisson's ratio v.

4. Numerical Analysis Using the Finite Element Method

For the numerical analysis using the finite element method (FEM), a 3x3 structure composed of 2D-DASS unit cells was designed in the SOLIDWORKS software package based on the geometric parameter values given in Table 1. The models with the non-optimized and optimized geometric parameter values are shown in Fig. 10 for the case of θ =50°.

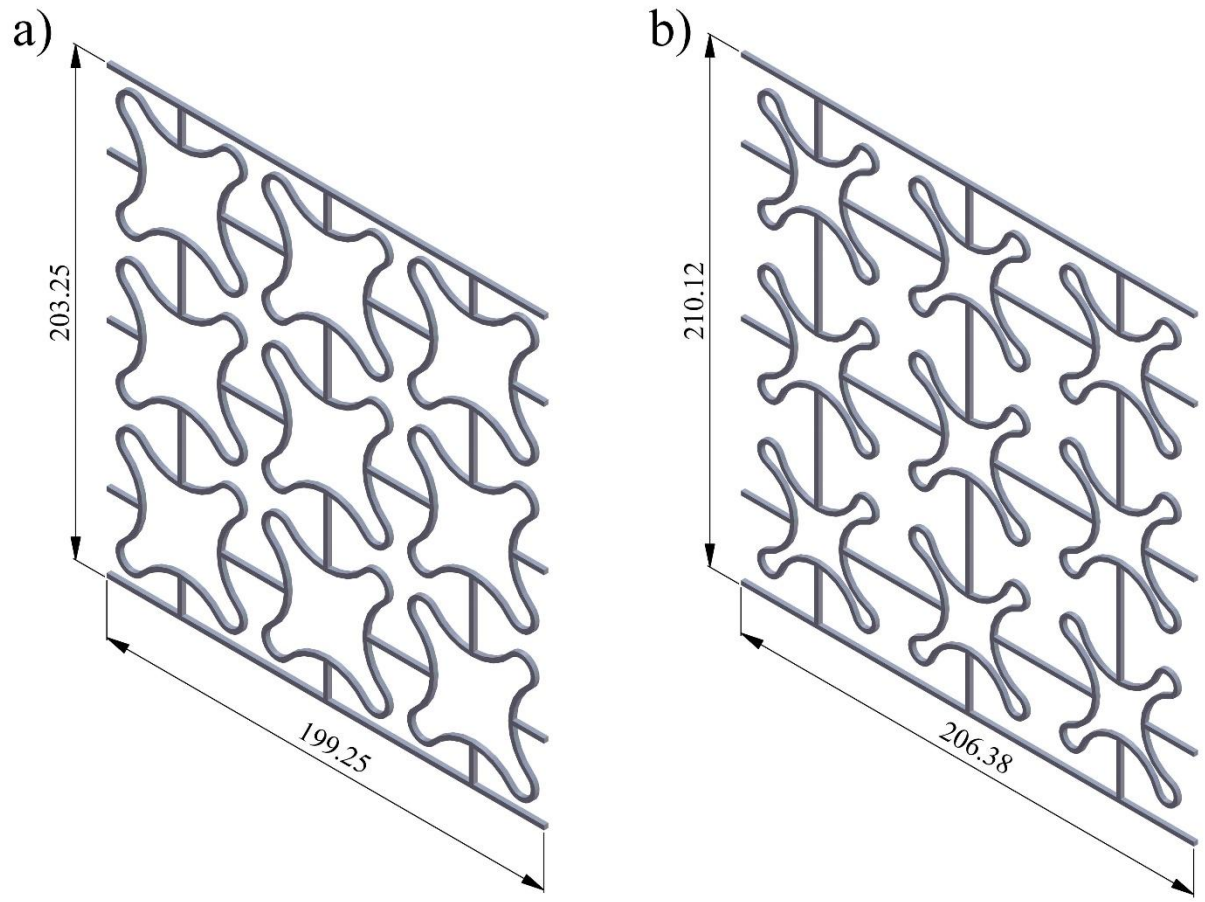


Fig. 10. 2D-DASS unit-cell structure for θ =50°: (a) non-optimized and (b) optimized.

For the numerical analysis using the finite element method (FEM), the Static Structural module of the ANSYS Workbench software package was employed. The numerical analysis was performed following the procedure described in [14]. The lower surface of the structure composed of 2D-DASS unit cells was fixed, while a prescribed vertical displacement was applied to the upper surface to simulate compression of the structure (Fig. 11). The simulation was performed using 15 load steps, with an end time of 1 s assigned to each step, during which the structure was subjected to a vertical displacement of 1 mm. Thus, the total prescribed vertical displacement was 15 mm. All constraints were defined as rigid. The output quantities obtained from the simulation were the vertical displacement of the upper surface, f_y, the horizontal displacements of the middle struts, denoted as f_x and $f_{x'}$ in Fig. 11, the vertical reaction force, and the total deformation. The material used in the simulation was polyamide 12 (PA2200), with a density of ρ_m=0.92 g/cm^3, Young's modulus of E_m=1500 MPa, and Poisson's ratio of v_m=0.4 [21].

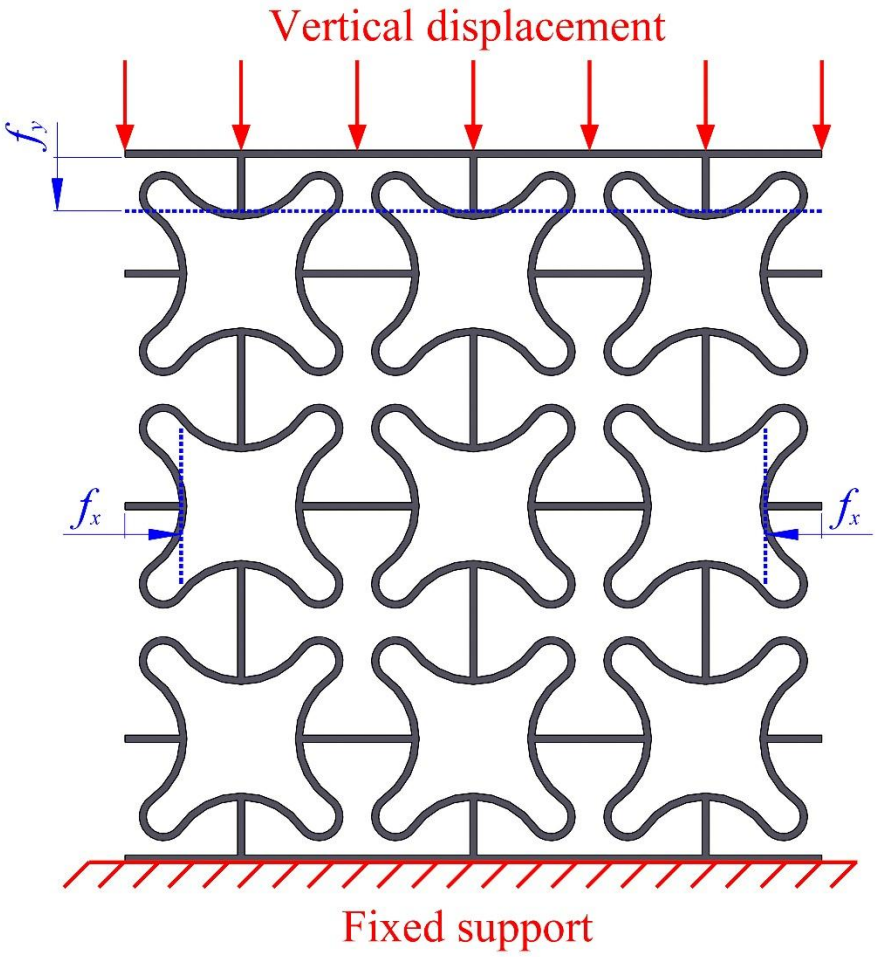


Fig. 11. Schematic representation of the simulation model.

The tetrahedrons method was used for the finite element type, with the patch conforming algorithm, while the element order was defined according to the global settings (Use Global Settings). To determine the appropriate finite element size, a mesh convergence study was performed for element sizes ranging from 2 mm to 0.3 mm, with an increment of 0.1 mm, for θ =55°. The criteria used for selecting the appropriate finite element size were the maximum vertical force at the final simulation step, the maximum horizontal displacement of the structure, and the skewness value. The skewness parameter is a measure of finite element quality and indicates the degree to which the shape of an element deviates from its ideal shape. The skewness value ranges from 0 to 1, where a value of 0 corresponds to an ideal element, whereas a value of 1 represents complete deviation from the ideal shape. According to the mesh quality criterion, skewness values ranging from 0 to 0.25 are considered excellent [32] .

Figure 12 presents the convergence curves of the obtained results as a function of the finite element size. As can be observed, the vertical force continuously decreases with decreasing finite element size. In contrast, for finite element sizes ranging from 2 to 1.4 mm, the horizontal displacement of the structure exhibits pronounced variations. In the range from 1.4 to 0.8 mm, these variations become considerably smaller, although more pronounced peaks can still be observed. In the range from 0.8 to 0.4 mm, the horizontal displacement becomes almost stable, with considerably smaller variations. Based on the results presented in Fig. 12, a finite element size of 0.6 mm was selected for the subsequent numerical analysis. For this element size, the skewness value falls within the range from 0 to 0.25 and is equal to 0.2368. Figure 13 shows the generated finite element mesh of the structure composed of 3x3 2D-DASS unit cells.

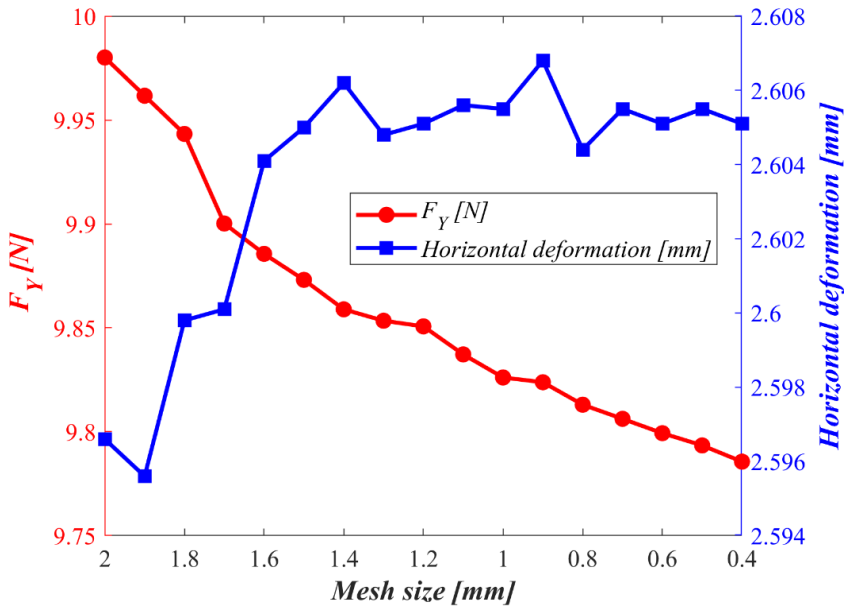


Fig. 12. Convergence analysis of the structure composed of 3x3 2D-DASS unit cells for θ =50°.

Figure 13 presents the total deformation distributions obtained from numerical simulations performed in ANSYS for the case of θ =55°. Figure 13(a) shows the non-optimized structure, whereas Figure 13(b) shows the optimized structure. The results clearly indicate that, for the same vertical deformation, the optimized structure exhibits greater horizontal deformation than the non-optimized structure, resulting in a greater absolute value of Poisson's ratio.

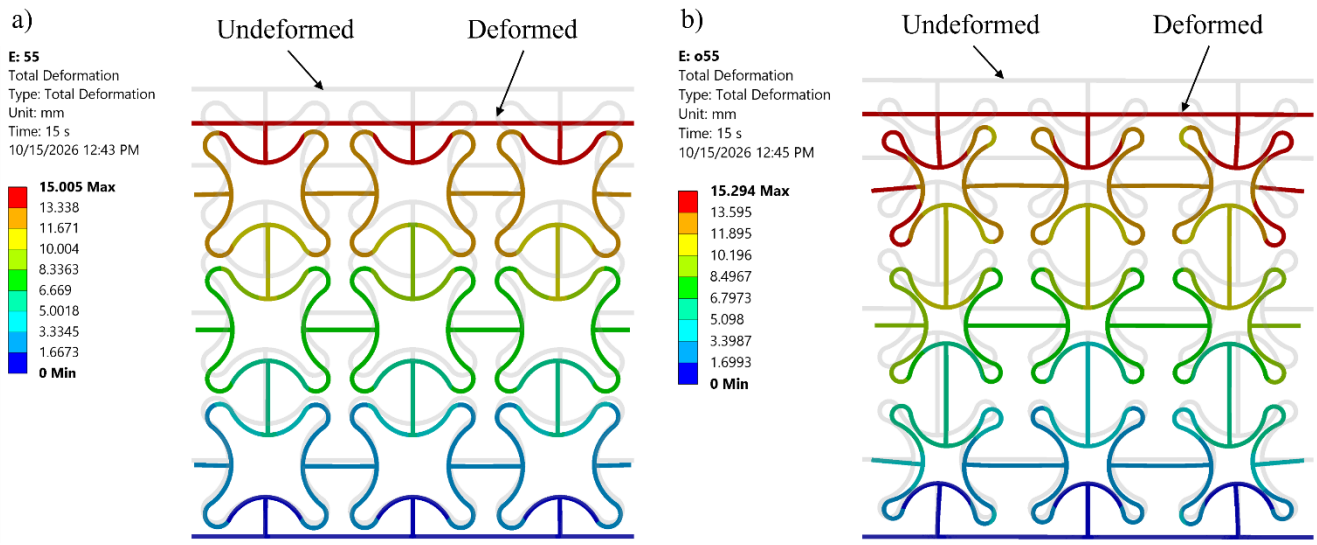


Fig. 13. Total deformation distributions obtained from numerical simulations for θ =55°: (a) non-optimized and (b) optimized.

In addition to the deformation results, the vertical forces obtained from ANSYS were compared between the non-optimized and optimized structures throughout the entire simulation. The force comparison diagrams are presented in Figure 14 for θ= 35°, 45°, 55° and 65°. For lower values of θ (Figures 14(a) and 14(b)), greater differences in vertical force are observed between the non-optimized and optimized structures. In contrast, for higher values of θ (Figures 14(c) and 14(d)), these differences are considerably smaller, and the vertical force values for the non-optimized and optimized structures are in close agreement.

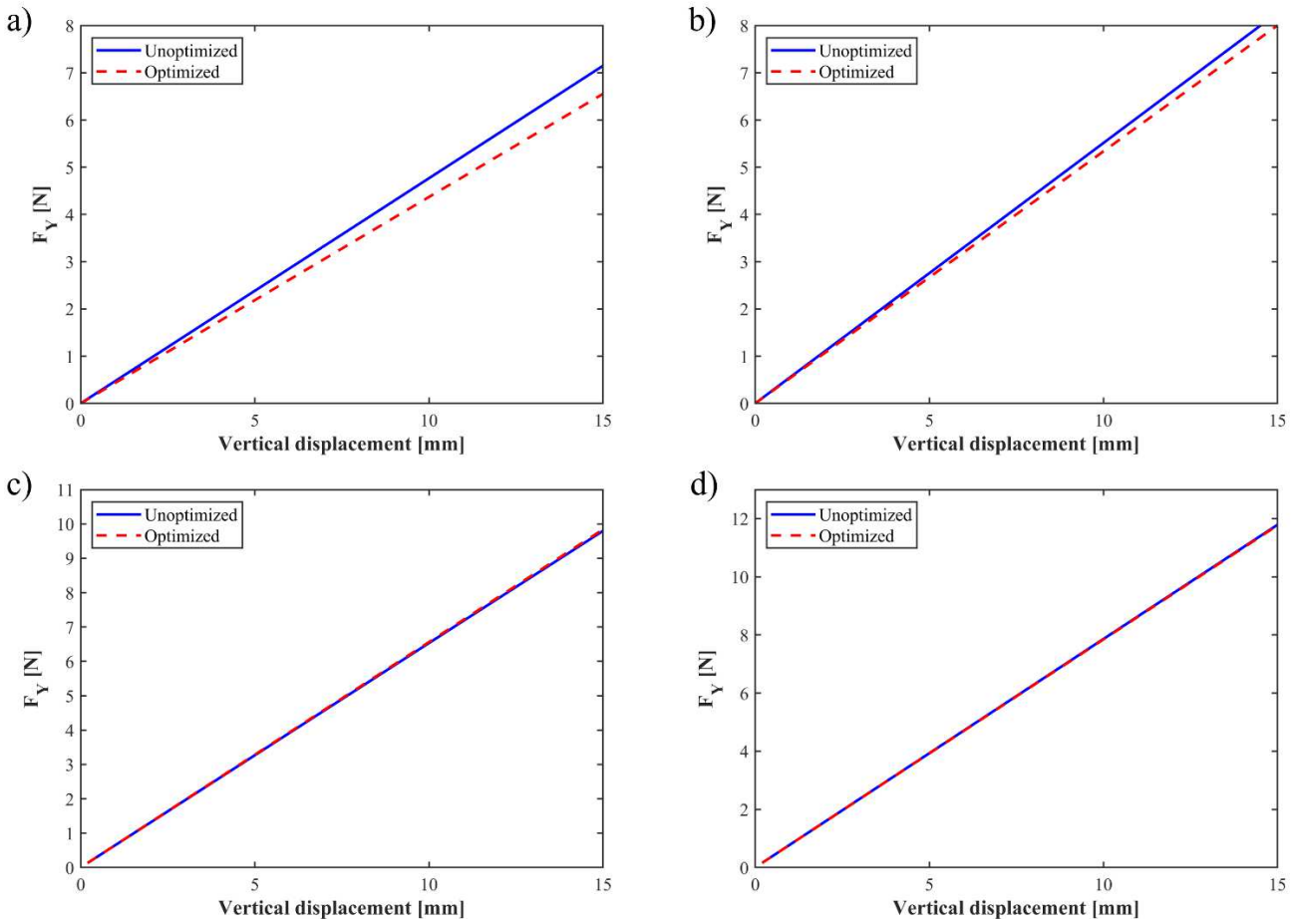


Fig. 14. Comparison of vertical forces obtained from numerical simulations for the non-optimized and optimized structures at θ: (a) 35°, (b) 45°, (c) 55° and (d) 65°.

Finally, Figures 15(a) and 15(b) present comparisons of Young's modulus E_Y and Poisson's ratio v, respectively, obtained using the analytical approach, the SEO optimization algorithm, and the numerical model. Figure 15 shows that the values obtained from the numerical simulations exhibit relatively small deviations from the analytical results and those obtained using the SEO algorithm.

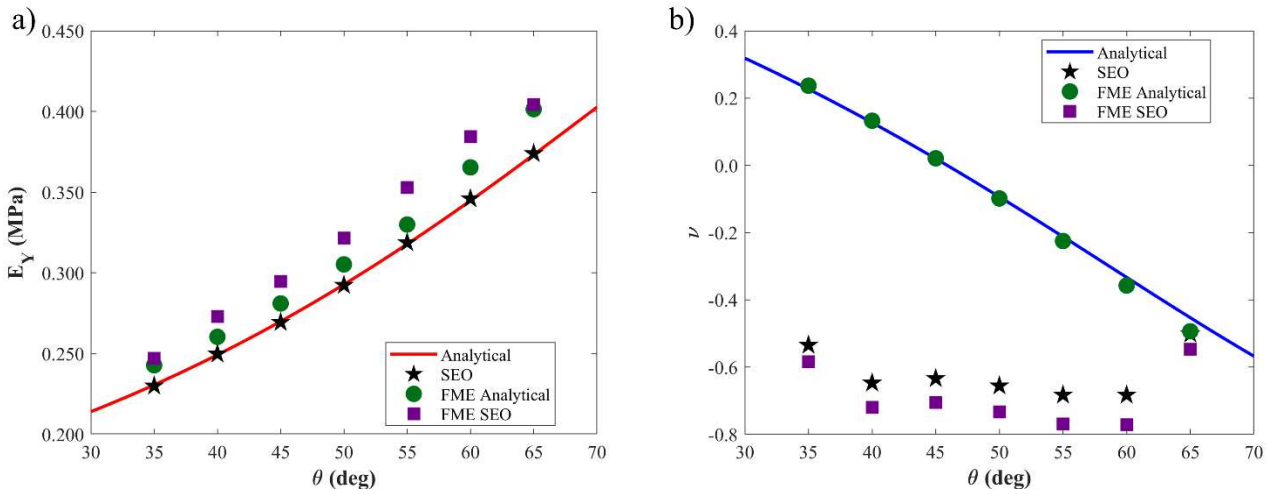


Fig. 15. Comparison of the analytical results, SEO optimization results, and numerical model results: (a) Young's modulus E_Y and (b) Poisson's ratio ν.

5. Conclusions

This study investigated the parametric optimization of a 2D double arc star-shaped (2D-DASS) unit cell with the aim of minimizing its Poisson's ratio while maintaining its Young's modulus, solid material volume, and total unit-cell volume within prescribed allowable deviations. An analytical model based on Castigliano's second theorem and Euler–Bernoulli beam theory was employed to determine the mechanical properties of the unit cell. The optimization procedure was subsequently applied to identify suitable combinations of geometric parameters that provide improved auxetic behavior while satisfying the defined constraints.

The analytical results showed that the Poisson's ratio of the 2D-DASS unit cell decreases with increasing angle θ, reaching zero at approximately 45. 8975°. The results also indicated that increasing this angle leads to an increase in both relative density and Young's modulus. These findings demonstrate the influence of the geometric parameters on the mechanical response of the unit cell and provide a basis for the subsequent optimization procedure.

The optimization results demonstrated that the applied SEO algorithm successfully identified feasible solutions with lower Poisson's ratio values for all considered initial configurations. In each case, the optimized angle reached the upper bound of the prescribed interval, namely 70°. Of particular significance is that, for the initial angles of 35°, 40°, and 45°, the optimization procedure transformed the initially positive Poisson's ratio into a negative value. At the same time, the constraints imposed on Young's modulus, solid material volume, and total unit cell volume were satisfied within the prescribed allowable deviation of ±0.5%. These results demonstrate the potential of the proposed optimization procedure to improve the auxetic response of the 2D-DASS unit cell while preserving its principal mechanical and geometric characteristics.

Finally, finite element analyses were performed on structures composed of 3x3 non-optimized and optimized 2D-DASS unit cells. The numerical results showed that the optimized configurations exhibited greater horizontal deformation under the applied vertical compression, indicating a more pronounced auxetic response. Comparisons of the vertical reaction forces, Young's modulus, and Poisson's ratio obtained from the analytical model, optimization procedure, and finite element simulations showed generally good agreement, although differences between the non-optimized and optimized configurations depended on the initial angle.

Overall, the results indicate that combining analytical modeling, constrained parametric optimization, and finite element analysis provides an effective approach for investigating and improving the mechanical properties of 2D-DASS unit cells. The proposed procedure enables the identification of geometric configurations with a more negative Poisson's ratio while maintaining the selected mechanical and geometric characteristics within strictly defined limits.

APPENDIX

The expressions for the coefficients C_{Xi} and C_{Yi}, derived in Section 2.1, are given as follows:

$$C_{X1} = \left(8g^2 - 32 - g^4 - 8(2+g)\theta - 4(2+g)^2\theta^2\right),$$
$$C_{X2} = \left(8 + 2(2+g)\theta + (4+g)\theta^2\right), \tag{A.1}$$

$$C_{X3} = \left(2\left(8-g^2\right)+4(2+g)\theta+(2+g)(4+g)\theta^2\right),$$

$$C_{X4} = \left(4+\theta\left(2+g+2\theta\right)\right),$$

$$C_{X5} = \left(12g\theta(1+\theta)+g^2\left(\theta^2-2\right)+24\left(2+\theta+\theta^2\right)\right),$$

$$C_{X6} = 4\left(\pi+4\theta\right)^2\left(\pi+\left(4+g\left(\pi-2\right)+\pi\right)\theta+4(1+g)\theta^2\right)\cos\theta,$$

$$C_{X7} = \theta\left(\pi+4\theta\right)\left(\left(2+3g\right)\pi^2+2\left(8+g\left(14+g\right)\right)\pi\theta-4\left(2+g\right)\left(\left(g-6\right)g-4\right)\theta^2\right)\cos\left(2\theta\right),$$

$$C_{X8} = 4\left(\pi+4\theta\right)^2\left(\pi+\left(4-2g+\pi\right)\theta+4\theta^2\right)\sin\theta,$$

$$C_{X9} = 2\left(\pi+2\left(2+g\right)\theta\right)\left(\begin{array}{l}\pi^2-4\left(g-2\right)\pi\theta+\left(4\left(g-2\right)^2+\left(1+g\right)\pi^2\right)\theta^2\\+8\left(1+g\right)\pi\theta^3+16\left(1+g\right)\theta^4\end{array}\right)\sin\left(2\theta\right),$$

$$\begin{aligned}C_{Y1} &= 16\left(8g^2-g^4-32\right)\theta^4+32\left(2+g\right)^2\left(6+g^2\right)\theta^6+\pi^4\left(\left(3+2g\right)\theta^2-2\right)\\&\quad+4\pi^3\theta\left(\left(12+g\left(9+g\right)\right)\theta^2-8\right),\end{aligned}$$

$$C_{Y2} = \left(4\left(g^2-8\right)+(2+g)\left(24+g\left(10+g\left(2+g\right)\right)\right)\theta^2\right),$$

$$C_{Y3} = \left(4\left(g^2-24\right)+\left(144+g\left(120+g\left(26+g\left(4+g\right)\right)\right)\right)\theta^2\right),$$

(A.2)

$$C_{Y4} = -2\left(\pi+4\theta\right)^2\left(\pi\left(\theta-1\right)+2\theta\left(g+2\theta-2\right)\right)\cos\left(\theta\right),$$

$$C_{Y5} = 2\theta\left(\pi+4\theta\right)\left(\pi-2\left(g-2\right)\theta\right)\left(\pi+2(2+g)\theta\right)\cos\left(2\theta\right),$$

$$C_{Y6} = 2\left(\pi+4\theta\right)^2\left(\pi\left(\theta+g\theta-1\right)+2\theta\left(g-2+2\left(1+g\right)\theta\right)\right)\sin\left(\theta\right),$$

$$C_{Y7} = \left(\pi+2\left(2+g\right)\theta\right)\left(\pi+\left(4-2g+\pi\right)\theta+4\theta^2\right)\left(\pi\left(\theta-1\right)+2\theta\left(g+2\theta-2\right)\right)\sin\left(2\theta\right).$$

Acknowledgements

This paper is a result of the research conducted within the project grant number 451-03-34/2026-03/200108 supported by the Ministry of Science, Technology and Innovation of the Republic of Serbia and the CEEPUS project grant “Building Knowledge and Experience Exchange in CFD - RS-1012-10-2425” supported by the Central European Exchange Program for University Studies.

References

[1] Lim T-C. Mechanics of Metamaterials with Negative Parameters. Singapore: Springer Singapore; 2020. https://doi.org/10.1007/978-981-15-6446-8.

[2] Hu Q, Zhang X, Zhang J, Lu G, Tse KM. A review on energy absorption performance of auxetic composites with fillings. Thin-Walled Structures 2024;205:112348. https://doi.org/10.1016/j.tws.2024.112348.

[3] Lim T-C. Auxetic Materials and Structures. Singapore: Springer Singapore; 2015. https://doi.org/10.1007/978-981-287-275-3.

[4] Ren X, Das R, Tran P, Ngo TD, Xie YM. Auxetic metamaterials and structures: a review. Smart Mater Struct 2018;27:023001. https://doi.org/10.1088/1361-665X/aaa61c.

[5] Hurairah MA, Lee S. Auxetic mechanical metamaterials (AMMs): A state-of-the-art review on advances in design, fabrication, and applications. Journal of Mechanical Science and Technology 2026;40:1093–122. https://doi.org/10.1007/s12206-026-0130-3.

[6] Periyasamy M, Srinivasan N. A review on auxetic structures: Applications, properties, classifications, finite element analysis, manufacturing methods, and selective laser melting process parameters. Results in Engineering 2025;28:107660. https://doi.org/10.1016/j.rineng.2025.107660.

[7] Momoh EO, Jayasinghe A, Hajsadeghi M, Vinai R, Evans KE, Kripakaran P, et al. A state-of-the-art review on the application of auxetic materials in cementitious composites. Thin-Walled Structures 2024;196:111447. https://doi.org/10.1016/j.tws.2023.111447.

[8] Wei L, Zhao X, Yu Q, Zhang W, Zhu G. In-plane compression behaviors of the auxetic star honeycomb: Experimental and numerical simulation. Aerosp Sci Technol 2021;115:106797. https://doi.org/10.1016/j.ast.2021.106797.

[9] Ai L, Gao X-L. An analytical model for star-shaped re-entrant lattice structures with the orthotropic symmetry and negative Poisson's ratios. Int J Mech Sci 2018;145:158–70. https://doi.org/10.1016/j.ijmecsci.2018.06.027.

[10] Zhang Z-Y, Li J, Liu H-T, Wang Y-B. Novel 2D arc-star-shaped structure with tunable Poisson's ratio and its 3D configurations. Mater Today Commun 2022;30:103016. https://doi.org/10.1016/j.mtcomm.2021.103016.

[11] Sinđelić V, Nikolić A, Minak G, Bogojević N, Ćirić Kostić S. An improved 2D arc-star-shaped structure with negative Poisson's ratio: In-plane analysis. Mater Today Commun 2023;37:107593. https://doi.org/10.1016/j.mtcomm.2023.107593.

[12] Liu H-T, Wang L. Design 3D improved star-shaped honeycomb with different tip angles from 2D analytical star-shaped model. Compos Struct 2022;283:115154. https://doi.org/10.1016/j.compstruct.2021.115154.

[13] Feng N, Tie Y, Guo R, Yuan Q, Xue F, Li C, et al. A concave four-arc honeycomb with enhanced stiffness and desirable negative Poisson's effect. Sci Rep 2023;13:21144. https://doi.org/10.1038/s41598-023-48570-y.

[14] Zheng Z, Chen D, Xie C, Li L, Lin C. In-plane analysis of an adjustable structure with negative Poisson's ratio and superior lightweight design. Smart Mater Struct 2025;34:075005. https://doi.org/10.1088/1361-665X/ade8bf.

[15] Zawistowski M, Poteralski A. Parametric optimization of selected auxetic structures. Multiscale and Multidisciplinary Modeling, Experiments and Design 2024;7:4777–89. https://doi.org/10.1007/s41939-024-00452-0.

[16] Zawistowski M, Poteralski A. Development of a hybrid material with auxetic phase. Multiscale and Multidisciplinary Modeling, Experiments and Design 2024;7:4767–75. https://doi.org/10.1007/s41939-024-00472-w.

[17] Liu H, Wei H, Zhao C. Multi-objective optimization of ASH-R and BRH-R metamaterials for near-zero Poisson's ratio and enhanced modulus. International Journal of Mechanics and Materials in Design 2026;22:145. https://doi.org/10.1007/s10999-026-09962-w.

[18] Chang Z-Y, Liu H-T, Cai G-B. Mechanical properties and prescribed design of a star-shaped re-entrant honeycomb based on multi-objective optimization. Mater Today Commun 2024;40:110091. https://doi.org/10.1016/j.mtcomm.2024.110091.

[19] Wang L, Liu H-T. Parameter optimization of bidirectional re-entrant auxetic honeycomb metamaterial based on genetic algorithm. Compos Struct 2021;267:113915. https://doi.org/10.1016/j.compstruct.2021.113915.

[20] Hamid U, Bai J, Kosec G, Wang L, Abdel Wahab M. Optimization of auxetic honeycomb structures for mechanical performance. Compos Struct 2025;371:119458. https://doi.org/10.1016/j.compstruct.2025.119458.

[21] Sinđelić V, Ćirić-Kostić S, Nikolić A, Bogojević N, Minak G. Parametric Optimization of an Auxetic Star-Shaped Structure using the Grey Wolf Optimizer (GWO) Algorithm. Mechanics of Solids 2026;61:120. https://doi.org/10.1134/S0025654425607244.

[22] Mirjalili S, Mirjalili SM, Lewis A. Grey Wolf Optimizer. Advances in Engineering Software 2014;69:46–61. https://doi.org/10.1016/j.advengsoft.2013.12.007.

[23] Kennedy J, Eberhart R. Particle swarm optimization. Proceedings of ICNN'95 - International Conference on Neural Networks, IEEE; n.d., p. 1942–8. https://doi.org/10.1109/ICNN.1995.488968.

[24] Deb K, Pratap A, Agarwal S, Meyarivan T. A fast and elitist multiobjective genetic algorithm: NSGA-II. IEEE Transactions on Evolutionary Computation 2002;6:182–97. https://doi.org/10.1109/4235.996017.

[25] Cotta C, Mathieson L, Moscato P. Memetic Algorithms. Handbook of Heuristics, Cham: Springer Nature Switzerland; 2025, p. 1–42. https://doi.org/10.1007/978-3-319-07153-4_29-2.

[26] Zavala AEM, Aguirre AH, Diharce ERV. Particle Evolutionary Swarm Optimization with Linearly Decreasing ε-Tolerance, 2005, p. 641–51. https://doi.org/10.1007/11579427_65.

[27] Takahama T, Sakai S. Constrained Optimization by ε Constrained Differential Evolution with Dynamic ε-Level Control. Advances in Differential Evolution, Berlin, Heidelberg: Springer Berlin Heidelberg; n.d., p. 139–54. https://doi.org/10.1007/978-3-540-68830-3_5.

[28] Sinđelić V, Ćirić-Kostić S, Nikolić A, Bogojević N, Minak G. Analytical and Numerical Approach for Determining the Mechanical Properties of a Novel 3D Double Arc Star-Shaped Structure with Two Different Cross-Sections. Mechanics of Solids 2025. https://doi.org/10.1134/S0025654425601958.

[29] Sinđelić V, Nikolić A, Bogojević N, Ćirić-Kostić S, Minak G. Analytical and numerical analysis of the modified 2D arc-star-shaped structure with negative Poisson's ratio. Engineering Today 2024;3:55–62. https://doi.org/10.5937/engtoday2400004S.

[30] Sebald A V., Fogel LJ. Evolutionary Programming. Evolutionary Programming, WORLD SCIENTIFIC; 1994, p. 1–386. https://doi.org/10.1142/9789814534116.

[31] Deb K, Pratap A, Agarwal S, Meyarivan T. A fast and elitist multiobjective genetic algorithm: NSGA-II. IEEE Transactions on Evolutionary Computation 2002;6:182–97. https://doi.org/10.1109/4235.996017.

[32] Orhan SN, Erden Ş. Numerical investigation of the mechanical properties of 2D and 3D auxetic structures. Smart Mater Struct 2022;31:065011. https://doi.org/10.1088/1361-665X/ac6918.